Ultraflexible organic light-emitting diodes for optogenetic nerve stimulation

Dongmin Kim[a], Tomoyuki Yokota[a], Toshiki Suzuki[a], Sunghoon Lee[a], Taeseong Woo[a], Wakako Yukita[a], Mari Koizumi[a], Yutaro Tachibana[a], Hiromu Yawo[b], Hiroshi Onodera[a], Masaki Sekino[a,1], and Takao Someya[a,1]

[a]Department of Electrical Engineering and Information Systems, Graduate School of Engineering, University of Tokyo, 7-3-1 Hongo, Bunkyo-ku, 113-8656 Tokyo, Japan; and [b]Department of Developmental Biology and Neuroscience, Graduate School of Life Sciences, Tohoku University, 2-1-1 Katahira, Aoba-ku, 980-8577 Sendai, Japan

Organic electronic devices implemented on flexible thin films are attracting increased attention for biomedical applications because they possess extraordinary conformity to curved surfaces. A neuronal device equipped with an organic light-emitting diode (OLED), used in combination with animals that are genetically engineered to include a light-gated ion channel, would enable cell type-specific stimulation to neurons as well as conformal contact to brain tissue and peripheral soft tissue. This potential application of the OLEDs requires strong luminescence, well over the neuronal excitation threshold in addition to flexibility. Compatibility with neuroimaging techniques such as MRI provides a method to investigate the evoked activities in the whole brain. Here, we developed an ultrathin, flexible, MRI-compatible OLED device and demonstrated the activation of channelrhodopsin-2–expressing neurons in animals. Optical stimulation from the OLED attached to nerve fibers induced contractions in the innervated muscles. Mechanical damage to the tissues was significantly reduced because of the flexibility. Owing to the MRI compatibility, neuronal activities induced by direct optical stimulation of the brain were visualized using MRI. The OLED provides an optical interface for modulating the activity of soft neuronal tissues.

optogenetic | organic electronics | flexible sensor

State-of-the-art electronics using organic semiconductors have enabled the fabrication of flexible and large-area electronic devices owing to the robustness of the organic material to bending (1–3). A variety of organic electronic devices, such as sensors (4–8), electrodes (9, 10), and light sources (11–13), can be fabricated on polymer films by using room-temperature solution processes, leading to the production of lightweight, thin, flexible, and large-area devices that are complementary to conventional silicon-based electronics (14). These emerging devices provide conformable interfaces between electronics and neuronal networks. For example, an organic transistor incorporating conductive polymer for recording human electroencephalograms is expected to be used in a brain–machine interface (5). Organic light-emitting diodes (OLEDs) have been utilized to produce flexible lighting and rollable displays (11–13). These days, the applications of OLEDs are now rapidly extending to wearable and biomedical applications (15–20). However, the applications of OLEDs in neuronal systems remain to be explored. The implementation of an OLED in neuronal devices, used in combination with animals that have been genetically engineered to include a light-gated ion channel (21–25), would enable cell type-specific neuron stimulation with conformal contact to a tissue surface. This technique would help stimulate the peripheral nervous system or the surface of the brain. In previous studies, miniature inorganic LEDs were implemented on flexible substrates to reduce the mechanical damage of tissue due to the implants (26–28). Park et al. (27) reported flexible neural probe arrays with illuminating dimensions 0.22×0.27 mm^2 and 1.6×0.8 mm^2 and light intensity above 10 mW/mm^2. These neuronal probes were encapsulated in elastomer to create a soft interface to tissues. Montgomery et al. (26) developed a fully implantable

inorganic LED stimulator with illuminating dimensions 0.32×0.25 mm^2 and light intensity 6 to 40 mW/mm^2. These inorganic stimulators maintained their illumination function for over 2 mo in saline solution or the body. Compared with these inorganic LEDs, the OLED device can be much larger because its light-emitting area is flexible. For such applications in optogenetics, the OLED should have an emission intensity sufficient to activate the light-gated ion channels. Owing to its ultrathin and nonmagnetic conductor layer, another potential advantage of the OLED is its compatibility with MRI. Functional MRI (fMRI) is an established technique used for mapping brain activities induced by stimulations (29, 30). However, conventional inorganic LEDs cannot be attached directly to the target neuronal tissues because inorganic LEDs generate MRI artifacts. The basic compatibility of OLEDs with MRI, such as potential interference with the MRI scan, remains to be investigated. Furthermore, point light sources such as optical fiber-coupled lasers or inorganic LEDs requires high light intensities to increase the population of stimulated neurons, which can cause thermal effects to the stimulated regions.

In this study, we developed an ultraflexible thin-film optogenetic stimulator using the OLEDs and demonstrated stimulation of the brain and peripheral nerves of a transgenic rat that expresses channelrhodopsin-2 (ChR2) in neurons (31–33). To activate neurons expressing ChR2, which requires a wavelength of ~480 nm (31), the emission spectrum of the OLED between

Significance

We have developed an ultraflexible and MRI-compatible optogenetic stimulator using organic light emitting diodes (OLEDs), which activate channelrhodopsin-2–expressing neurons in transgenic animals. The OLEDs can be conformally attached to soft neuronal tissues, such as peripheral nerves or brain, and the superior mechanical flexibility significantly reduces mechanical damages to the tissues. They are also compatible with neuroimaging techniques such as MRI, while allowing investigation of the evoked activities induced by optical stimulations without artifact effects. Finally, we have successfully demonstrated the optical stimulation of the peripheral nerves and the brains of rats and visualized the evoked neuronal activities induced by optical stimulations using the functional MRI.

400 and 580 nm was used. A light power density of 0.5 mW/mm^2 was sufficiently high to drive the OLED over the animal's relatively low nerve-excitation threshold of ∼0.3 mW/mm^2, which was achieved in our original animal strain expressing ChR2 in all neurons in the body (32). Using the OLED, we were able to stimulate peripheral nerves because of its stable and conformal contact to the body, and we unambiguously demonstrated neuronal excitations. An attached OLED applied optical stimulation to the brain, and the induced brain activities were observed using MRI.

Results

The OLED device has three emission areas on a thin-film structure (Fig. 1A). Each OLED cell has stacked layers of a buffer layer, an active layer, and a hole transport layer between an Al cathode electrode and an indium tin oxide (ITO) common anode electrode (Fig. 1B). Considering relatively high resistance of ITO, the common anode electrode was fabricated with a two-layer design: a continuous layer of ITO and a layer of gold patterned outside the OLED light-emitting areas (*SI Appendix*, Fig. S1A). By introducing an additional gold-wiring layer, we modified the emitted light power to ∼40% higher than that of the single ITO wiring layer (*SI Appendix*, Fig. S1B). The size of each emission area is 2 mm × 2 mm and the center-to-center distance is 4 mm.

The total thickness of the device is only 2 μm. The details of the device structure and the fabrication process are described in *Materials and Methods*. The OLED was fabricated on a glass plate and delaminated for use. The delaminated OLED device (Fig. 1C) is flexible and robust against deformations (Fig. 1D), emitting light even when placed around a thin tube and has a bending radius of less than 50 μm (*SI Appendix*, Fig. S1C). Tolerance to the repeated bending was evaluated in our previous study (12). The light distribution did not significantly change before and after the delamination (Fig. 1E). The emission spectrum is distributed in the wavelength range from 400 to 580 nm, and the peak intensity occurs at a wavelength of around 455 nm. This emission characteristic wavelength range of 470 to 480 nm is appropriate to activate neurons expressing ChR2 (24–28). The external quantum efficiency (EQE) was ∼6% and the current was ∼58 mA at direct current (DC) driving voltage of 10 V (Fig. 1F). A pulse-like driving method of the OLED can reduce thermal damage to the organic layer and improve the illuminance and the optical-power density (16). The current reached ∼120 mA at the driving voltage of 20 V with pulses of 5 ms (*SI Appendix*, Fig. S1D). The intensity profiles of the light output from the OLED shows Lambertian emission (*SI Appendix*, Fig. S1E) and the luminance reached 4.3 × 10^4 Cd/m^2 at 10 V. (*SI Appendix*, Fig. S1 F and G). The resulting optical-power density measured by facing
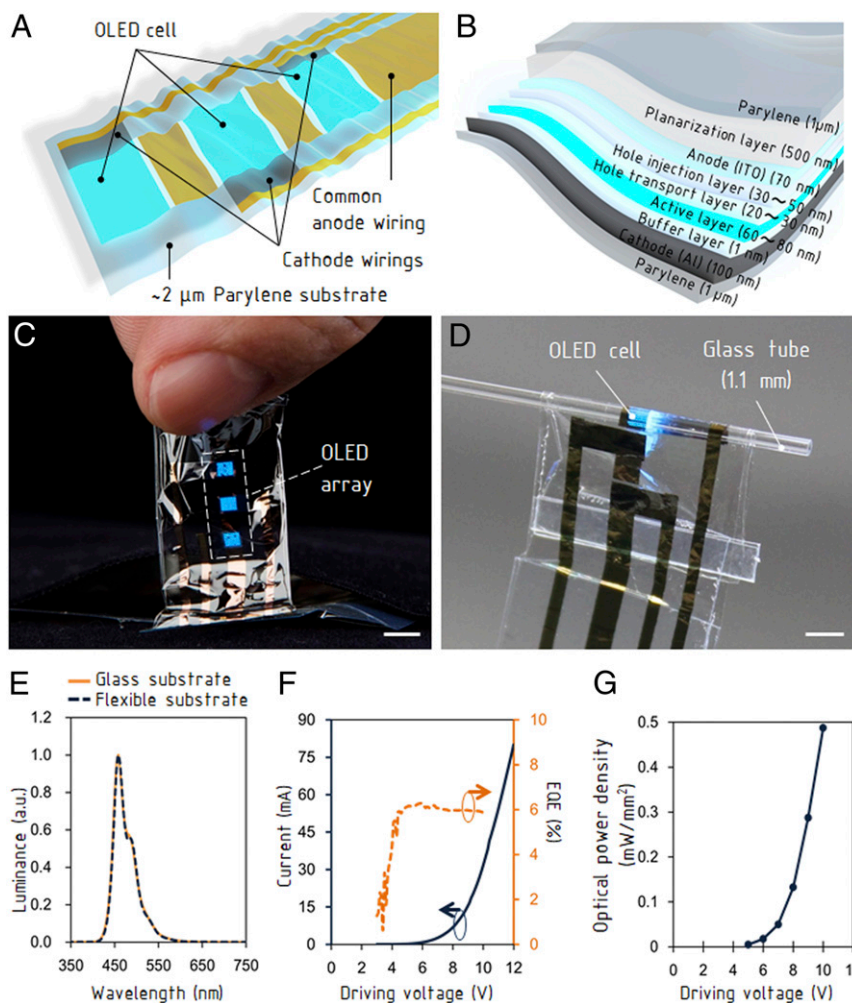

Fig. 1. Structure and characteristics of ultraflexible OLED device. (A) Structure of the OLED device with three emission cells and wirings. (B) Cross-sectional view of the emission cell. (C) Photograph of the OLED detached from the supporting glass substrate. (Scale bars, 4 mm.) (D) Light emission from the bent OLED. (Scale bar, 2 mm.) (E) The electroluminescence spectra of the OLED. a.u., arbitrary units. (F) The I-V characteristics and the external quantum efficiency of the OLED. (G) The optical-power density against the driving voltage.

a photodiode was ~0.5 mW/mm^2 (Fig. 1G). The lifetime of the OLED is an important issue for an optogenetic application. Although half-life time of OLEDs under the brightness of 1,000 cd/m^2 is only 3 h, 1-μm-thick parylene encapsulation layer (Young's modulus of paryelene is 2.8 GPa) can extend the lifetime to 5.5 h (*SI Appendix*, Fig. S1*H*). Furthermore, when the OLED was driven by a pulsed voltage of 15 V with pulse duration 5 ms and frequency 2 Hz for 14 h (*SI Appendix*, Fig. S2*A*), the brightness was maintained above ~80% (*SI Appendix*, Fig. S2*B*). On extracted muscle tissue, the brightness of the OLED was maintained above ~95% for ~3 h, which represents the stability of the OLED under in vivo conditions, and dropped sharply (*SI Appendix*, Fig. S2*B*). Each experiment using flexible OLEDs was performed within 1 h using a new OLED. The OLED consists solely of nonmagnetic materials and the conductive layer was fabricated with a thickness less than the skin depth at the Larmor frequency of the MRI (300 MHz at 7 T). This effectively prevents interference with main magnetic field and RF field in the MRI system (34).

The W-TChR2V4 transgenic rat (31–33, 35) expressing ChR2 was used for the following three animal studies: muscle contractions
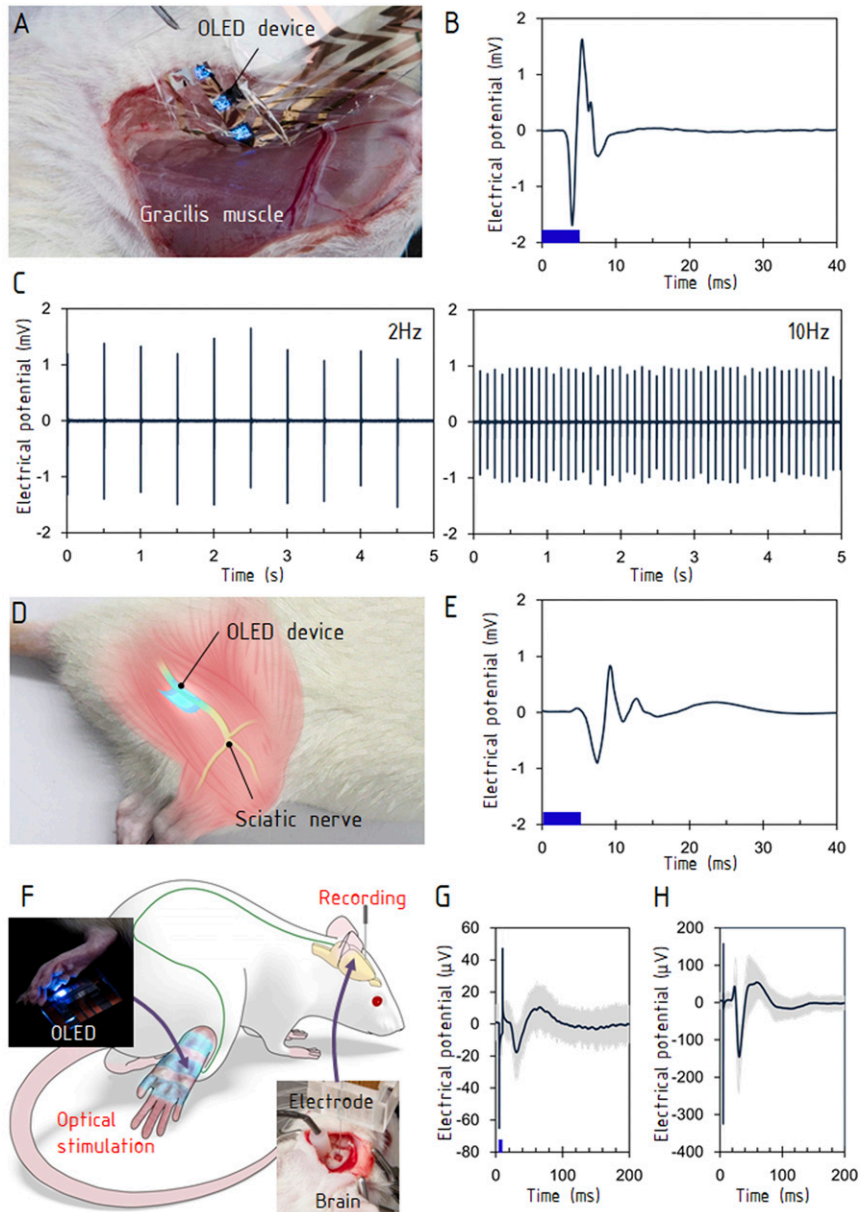

Fig. 2. Stimulations of motor and sensory systems. (*A*) The OLED was attached to a surface of gracilis muscle (*Materials and Methods*). (*B*) The evoked electromyogram. The stimulation frequency was 10 Hz, and the data were averaged over 10 stimulations. (*C*) The evoked electromyograms at 2 and 10 Hz. (*D*) The OLED was placed on the exposed sciatic nerve of the hindlimb. (*E*) The evoked electromyogram at the gastrocnemius muscle. The stimulation frequency was 10 Hz, and the data were averaged over 10 stimulations. (*F*) The experimental setup for stimulating sensory neurons in the hindlimb and recording the somatosensory evoked potential in the brain. The lower right photograph shows the needle electrode inserted into the primary somatosensory cortex (S1) contralateral to the stimulated hindlimb. The upper left photograph shows the OLED attached to the hindlimb. (*G*) Electrical potentials evoked by optical stimulations. The first negative peak occurred ~25 ms after stimulation, and the peak pair at <10 ms was an artifact caused by the stimulation. (*H*) Evoked potentials by electrical stimulations to the hindlimb. The stimulus intensity and duration were 0.7 mA and 300 μs, respectively. The blue bars in *B*, *E*, and *G* show the durations of optical stimulations (5 ms).

evoked by nerve stimulations, the stimulation of sensory neurons, and visualization of evoked brain responses using MRI. To demonstrate optically induced muscle contractions, the OLED was attached to a nerve terminal of the gracilis muscle of the hindlimb (Fig. 2*A* and *SI Appendix*, Fig. S3*A*). The current–voltage (I-V) characteristics of the OLED did not vary before or after attachment to the muscle (*SI Appendix*, Fig. S3*B*). This indicates that the leakage current was negligibly small because of the device's durable encapsulation. When the OLED was driven by pulses of 5 ms with an amplitude of 15 V, the myoelectric potential measured on the gracilis muscle revealed that stable tensional responses were evoked 4 ms after the optical stimulation (Fig. 2*B*). During optical stimulation with repetition rates ranging from 2 to 40 Hz, hindlimb movement was induced in synchronization with the optical pulses (Fig. 2*C* and Movie S1). At frequencies of 20 Hz and 40 Hz, the contraction diminished because of desensitization (36) (*SI Appendix*, Fig. S3*C*). Even during the contraction, the OLED delivered stable optical stimulations because of its high conformity to the muscle surface. A conformal contact to the tissue is beneficial when the stimulations cause deformation of the tissue, which occurs in muscles and peripheral nerves. The leakage current from OLED was negligibly small (*SI Appendix*, Fig. S3*D*). A further experiment was carried out using an OLED on a glass plate. The glass plate was effective at separating the optical stimulation from thermal and electrical effects and bypassed the need for delamination of the ultrathin OLED, which is a low-yield process. The glass substrate is not essential for practical applications, as demonstrated in Fig. 2 *A–C*. The OLED was placed on a portion of the sciatic nerve that was surgically isolated from surrounding tissue (Fig. 2*D*). Optical stimulations were delivered for a duration of 5 ms. The myoelectric potential showed that optical stimulation of the sciatic nerve evoked a contraction of the gastrocnemius muscle (Fig. 2*D* and Movie S2). This neuronal activation was caused solely by optical emission, rather than by heating from the OLED or leakage current. To confirm that this muscle contraction was not caused by any thermal effect, we irradiated the sciatic nerve with a 580-nm laser (*SI Appendix*, Fig. S4*A*), which gave a thermal input but did not activate ChR2. No muscle contraction was observed at the intensities as high as 11.2 mW (*SI Appendix*, Fig. S4 *B* and *C*). As another evaluation of thermal effect, OLED stimulation was applied to a wild-type animal. Again, no muscle contraction was observed (*SI Appendix*, Fig. S4*D*).

To demonstrate optogenetic stimulation of the sensory neurons, the OLED was attached to the plantar skin, and the evoked potential was measured at the somatosensory cortex (Fig. 2*F* and Movie S3). The glass plate was again placed between the OLED and the skin for thermal and electric insulation. The OLED was driven with pulse durations of 5 and 10 ms at the pulse amplitude of 15 V. The two responses in the somatosensory cortex evoked by optical stimulation and electrical stimulation exhibited a pair of consecutive negative and positive peaks; the latency of the first negative peak was ∼25 ms (Fig. 2 *G* and *H* and *SI Appendix*, Figs. S5 and S6). The peak amplitude was ∼25 μV under a stimulus pulse duration of 5 ms. A longer pulse duration of 10 ms induced a stronger response in the electrical potential (*SI Appendix*, Fig. S6*B*).

A major improvement of the OLEDs over other optical emitters is the significantly reduced mechanical damage to neuronal tissues because of their extraordinary flexibility. To evaluate the mechanical damage, we implanted a 5-mm-long cuff representing a rigid optical emitter and the OLED around the sciatic nerves for 10 d (*SI Appendix*, Fig. S7 *A* and *B*) and then histologically examined the nerve tissues (Fig. 3 *A* and *B*). In the nerve with the rigid cuff, damage to the myelin sheaths was observed on a histological specimen stained with Luxol fast blue (Fig. 3*A*). Expression of the macrophage/monocyte-specific protein CD68 also increased in the nerve with the rigid cuff (*SI Appendix*, Fig. S3 *B* and *C*). These results indicate that the nerve received repetitive mechanical stress from the rigid cuff. The

nerve with the OLED exhibited neither significant morphology change in the myelin sheaths nor CD68 expression. The OLED caused almost no mechanical stress to the nerve tissues.

We evaluated artifact effects in acquired MRI images around commercial GaN LEDs and developed OLED. A reference device was fabricated with conventional miniature GaN LEDs implemented on a flexible substrate. MRI scans were performed after attaching the GaN LEDs and the OLED to the surface of a perfusion-fixed rat brain (Fig. 3*D*). Signal loss occurred at a radius of ∼10 mm around the GaN LED due to its high electrical conductivity and high magnetic permeability. Even though the GaN LED does not include any circuit wiring, the artifact was observed. However, in the image acquired with the OLED, there was no interference with the MRI acquisition (Fig. 3*D* and *SI Appendix*, Fig. S8 *A* and *B* and *Supplementary Text*). The signal attenuation caused by the OLED was only 5% in a close proximity to the device (*SI Appendix*, Fig. S9 *A* and *B*). This MRI compatibility is a remarkable advantage of the OLEDs for applications in neuroimaging, because most electronic devices should be placed away from the sample to prevent artifacts appearing in images. As far as we know, no previous LED has been completely free from artifacts (*SI Appendix*, Fig. S9*C*).

With the free-standing OLED attached to the dura mater in living rat brain, we performed fMRI scans of the optically evoked activity. The OLED was driven with pulses of 5 ms, 10 V, and 3 Hz during fMRI scans. The measured optical-power density after the fMRI scan was 0.5 mW/mm^2 (total optical power of 2 mW) at DC 10 V driving voltage. The blood oxygenation level dependent (BOLD) response was observed locally in the stimulated sensorimotor cortex, which demonstrates the high MRI compatibility of the OLED (Fig. 4*A*). The stimulation also induced a BOLD response in the thalamus (25). The electromyographic signals recorded at the forelimb exhibited periodical pulses in synchronization with the optical stimulations, indicating that the cortical OLED stimulations induced electrical activity in the motor neurons (*SI Appendix*, Fig. S10 *A* and *B*). Our study demonstrates an MRI scan of a brain in the presence of an implant OLED.

The OLED is a unique device providing an area light source of 2 mm × 2 mm, whereas existing devices such as optical fibers provide point light sources (Fig. 4*B*). The resulting benefit is an increased population of stimulated neurons due to the increased emitting area. While the OLED evoked a clear BOLD response at a total optical power of 2 mW (Fig. 4*A*), the fiber-coupled laser stimulations induced detectable BOLD responses at 12 mW and above (Fig. 4*C*). The targeted sensorimotor cortex exhibited a clear activation at 20 mW. The BOLD responses in the contralateral cortex are caused by the functional interhemispheric connections of the sensorimotor cortex (37, 38). The relatively weak BOLD signal at the sensorimotor cortex is attributable to a magnetic-susceptibility effect at the air–tissue boundary. The improved homogeneity of illumination across the large area by the OLEDs allows us to simultaneously stimulate many neurons at the same light intensities just above the threshold, whereas point light sources require higher light intensity to increase the population of stimulated neurons. Subsequently, our approach also relieves the focal heating of neuronal tissues caused by absorption of excessive intense light (39, 40). The absorption coefficient of tissues is as large as 0.07 mm^{-1} at a wavelength of 470 nm (41). Therefore, a critical technical challenge when using point light sources is the thermal effects on neuronal tissues at the emitter tip, resulting from a locally high optical-power density. The temperature increase caused by continuous illumination for 90 s with a light power of 2 mW was measured using a thermocouple (XQ-213-RS; RS PRO) directly in contact with the extracted brain tissue. The temperature increased by ∼0.3 °C by the OLED and ∼3.2 °C by an optical fiber of 250 μm in diameter (Fig. 4 *D* and *E*).
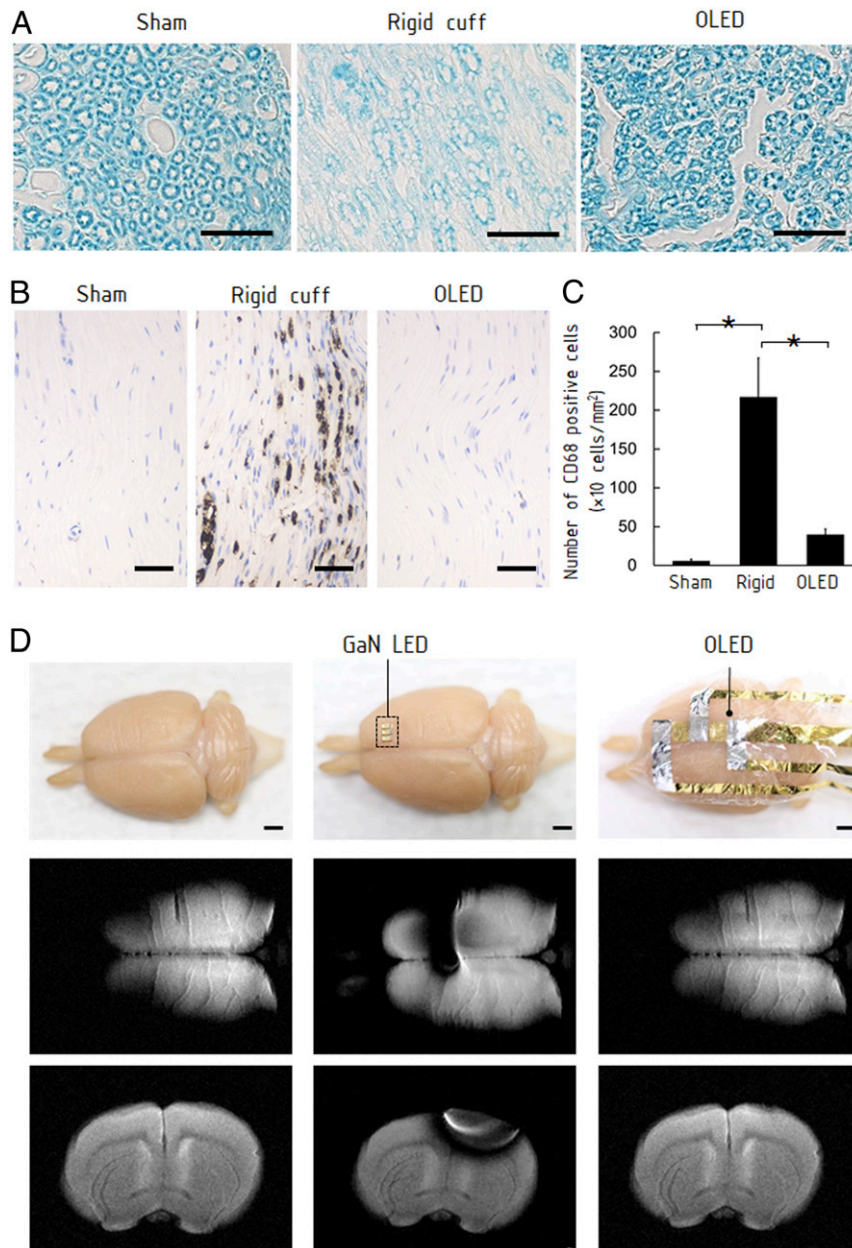
Fig. 3. Characterization of OLED attached on neuronal tissues. (*A*) Histological sections of sciatic nerves with a cuff representing a rigid optical emitter and the OLED attached around the nerve for 10 d (*Materials and Methods*). The transverse section stained with Luxol fast blue exhibits significant morphological change of the myelin sheath when the rigid cuff was attached. There was no clear difference between the nerve with the OLED and the sham-operated nerve. (Scale bars, 20 μm.) (*B*) CD68 immunostaining on the longitudinal sections. The nerve with the rigid cuff exhibited overexpressed CD68, suggesting damage to the nerve. The nerve with the OLED did not exhibit overexpression. (Scale bar, 50 μm.) (*C*) The number of CD68-positive cells per unit area (cells per square millimeter) in each group (sham, rigid cuff implantation, and OLED implantation). Data are presented as means ± SEM. Asterisk denotes statistically significant differences across the groups (one-way ANOVA, $F = 7.32$, $P = 0.02$; Tukey–Kramer HSD test, $P < 0.05$). (*D*) MRI of a perfusion-fixed rat brain and the brain with attached conventional GaN LED and OLED. (Scale bar, 2 mm.) While the GaN LED caused an artifact, the influence of the OLED was negligible.

Illumination from the optical fiber at 2 mW did not cause any detectable rise in temperature, but illumination over 5 mW caused a higher rise in temperature than the OLED (Fig. 4*D*). Under a practical driving condition of the OLED at the frequency of 20 Hz with pulses of 5 ms and 15 V, the temperature increase was ∼0.1 °C after 5 min (*SI Appendix*, Fig. S11). Comparing the evoked BOLD response and the temperature rise between the OLED and fiber-coupled laser, we have demonstrated that the OLED is advantageous because it provides stronger BOLD responses with reduced heating. The improved

homogeneity of light intensity in the OLED is effective for avoiding hot spots in the tissues.

Discussion

In previous studies using rigid LEDs, mechanical stress to the neuronal tissues has been eliminated by reducing the size of LED or by placing an elastomer on the surface of the LED (26, 42–45). Recently, optical stimulation using miniature OLEDs was performed based on this approach, resulting in a spatial resolution of ∼55 μm² (18). Considering the tradeoff between
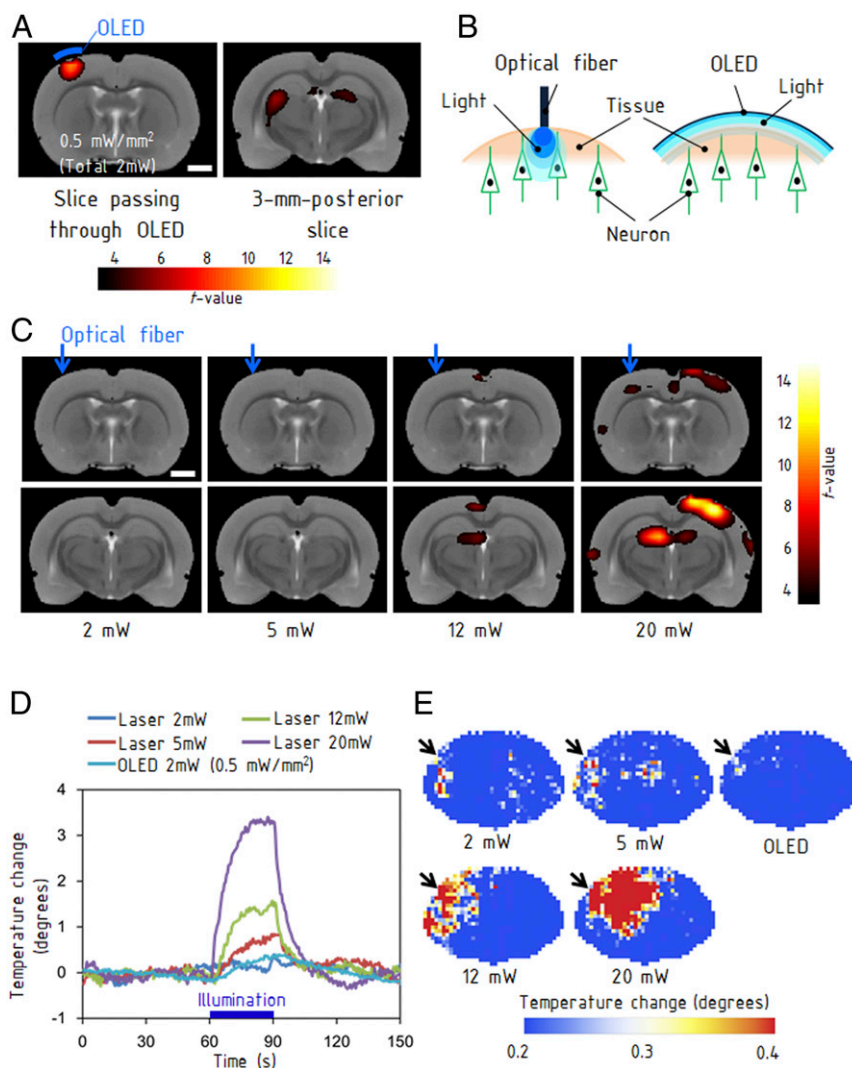
Fig. 4. MRI of brain activities evoked by optical stimulations. (*A*) The left map shows activation in the sensorimotor cortex, which was located immediately below the OLED emission area (*Materials and Methods*). The right map shows the induced activation in the thalamus 3 mm posterior to the stimulated area. (Scale bars, 2 mm.) (*B*) Difference between the OLED providing an area light source and an optical fiber providing a point light source. (*C*) fMRI obtained with stimulations from a fiber-coupled laser with light powers ranging from 2 to 20 mW. BOLD responses were evoked at 12 mW and higher. The images in the bottom row are at 3 mm posterior from the images in the top row. (Scale bars, 2 mm.) (*D*) Rise in temperature caused by illumination with the OLED and fiber-coupled laser. The measurements were performed on a rat brain with a craniotomy of 4 mm × 4 mm using a thermocouple. (*E*) Thermographs for each light power. The illumination using the optical fiber generated a hot spot, whereas the OLED caused a much smaller thermal effect. The measurements were performed using an extracted brain.

the focality of stimulation and the population of excited neurons, these miniature LEDs are suitable for delivering lights to small specific group of neurons. On the other hand, our device has flexible light-emitting areas (*SI Appendix*, Fig. S12 *A* and *B* and *Supplementary Text*). One of the advantages of an OLED is its ability to illuminate a large area with a high homogeneity that has hardly been achieved using arrayed micro-LEDs. Light-gated ion channels have recently been introduced to primates whose brains are larger than those of rodents. Several studies have suggested that larger emission areas in the brain are necessary for inducing behavioral changes in primates compared with rodents (46–49). In these applications, delivering light to an ensemble of neurons requires a millimeter-scale emission area. Since the size of a light-emitting area is adjustable, the OLED is applicable also to a focal stimulation. Furthermore, recent developments on quantum dot LEDs (QD-LEDs) have significantly improved the mechanical flexibility and demonstrated

flexile and large-area optical stimulators (50, 51). Although there are still challenges to implementing existing QD-LEDs to biological applications due to the use of toxic materials, they might also provide such possibilities as large-area and ultraflexible optical simulators.

In practical neuroscience applications of the OLED, the MRI compatibility is essential for visualizing the evoked brain activities. The OLED consists of nonmagnetic materials and the conductive layer can be thinner than the skin depth of the RF field in an MRI system (*SI Appendix, Supplementary Text*). This unique feature of the OLED, unlike conventional LEDs, leads to the MRI compatibility. Since MRI compatibility is a consequence of using thin metal layers, there is a tradeoff between the reduction of the wiring resistance and improving MRI compatibility. This is an important issue for future development. Providing low-pass filter characteristics to the wiring would be effective for maintaining the low resistance to the OLED

driving current and for reducing the effect on the MRI Larmor frequency.

The applications of optogenetics have recently been extended to cover the differentiation of stem cells (52). Optogenetic differentiation was also induced in immature myotube cells to obtain contractile ability, which has future applications in treating muscular and neurological disorders such as muscular dystrophy and amyotrophic lateral sclerosis (53). Future clinical application of these techniques requires the differentiation of massive stem cells into specialized cells, and the areal light source is suitable for in vivo differentiation. When the stem cells are differentiated at a target location in the body, a flexible light source applicable to curved surfaces is required. The OLED is suitable for delivering uniform illumination for efficient differentiation.

Improving the encapsulation of OLEDs is an important technical challenge for realizing a variety of practical applications in view of their long-term stability. Hybrid organic–inorganic thin-film encapsulations have recently been developed, and a sufficiently low water-vapor transmission rate of 10^{-6} has been reported. Introducing this type of encapsulation, in addition to the use of thicker layers, would lead to an improved lifetime of flexible OLEDs. To use the OLED in fully implantable optogenetic studies, a wireless power transmission system (27) must be combined with the improved encapsulation layer. The relatively high driving voltages that limit the power efficiency of the OLED stimulators must also be improved by reducing the wiring resistance. While conventional rigid GaN LEDs show EQEs above 50%, the EQE of the OLED was ~6%. However, the performance of OLEDs is still being improved owing to novel principles and materials. A recently developed blue OLED has achieved an EQE above 20%, although its stability must be improved. Further development of the materials would lead to lower voltage and lower power consumption. Monitoring the thermal effect caused by the power consumption is an issue in optogenetic stimulations. The processing technology introduced in this study is also applicable to the implementation of a resistive thermistor on the OLED. Despite these issues, we believe that a long-term implantable OLED stimulator will be beneficial as a soft optical interface for optogenetic applications.

Materials and Methods

Fabrication of the OLED Device. The fabrication of ultraflexible OLED was published in another paper (12). A 1-μm-thick Parylene diX SR layer was formed on the 0.7-mm-thick supporting glass plate as an ultrathin substrate by chemical vapor deposition. The surface of glass was treated by fluoric polymers (Novec 1700; 3M Company) for an easy delamination of ultraflexible OLEDs after the manufacturing. Then, a 500-nm-thick polyimide planarization layer (KEMITITE CT4112; Kyocera Chemical) was deposited on a parylene substrate by spin-coating (4,000 rpm, 60 s) and cured at 90 °C for 1 h, 120 °C for 1 h, and 150 °C for 1 h in nitrogen. First, the 70-nm-thick ITO anode was formed by sputtering, and the electrode layer was patterned by photolithography and a wet etching process. Subsequently, 100-nm-thick Au electrodes were deposited as wiring. Next, the hole injection layer (Plextore Organic Conductive Inks; Sigma-Aldrich Co. LLC) and hole transport layer (STSIL010, Sumitomo Chemical Co., Ltd.) were formed on the anode by spin-coating, and the device was then annealed in the atmosphere and nitrogen, respectively, where the maximum process temperature was 180 °C. Then, a 60-nm-thick fluorescent polymer (STSB010; Sumitomo Chemical Co., Ltd.) was formed between the sodium fluoride (NaF)/aluminum (Al) cathode and the device was annealed at 150 °C in nitrogen. This material consists of a conjugated polymer system with fluorenes, phenylenes, and other poly-condensed aromatic compounds as basic units, as well as emitting moieties in the polymers. The thicknesses of the aluminum, ITO, and gold electrodes were 200, 70, and 100 nm, respectively. Finally, the device was encapsulated by a 1-μm-thick Parylene diX SR layer. Two types of wiring (one-layered and two-layered) were fabricated to compare the performances. The one-layered wiring consisted of 70-nm-thick ITO, and the two-layered wiring consisted of 100-nm-thick gold and 70-nm-thick ITO. Cu cables were directly

attached to the Au contact pad on the ultrathin substrates using surgical adhesive tapes (KEEP PORE A; NICHIBAN).

Measurement for the Characterization of the OLEDs. Measurements of the fundamental characteristics of the OLED were performed before it was detached from the supporting glass plate. The emission spectra of the OLED (Fig. 1E) were measured by a brightness light-distribution characteristics measurement system (C9920-11; Hamamatsu Photonics K.K.). In addition, the emission spectra of the free-standing OLED were also evaluated. The I-V curves, quantum efficiencies (Fig. 1F), and luminescence (*SI Appendix*, Fig. S1F) were measured on the glass plate by an external quantum efficiency measurement system (C9920-12; Hamamatsu Photonics K.K.). The emission power of the OLED was measured using a light power meter (Nova, P/N 7Z01500; OPHIR) equipped with a photosensitive diode (PD300-1W; OPHIR) (Fig. 1G). The photosensitive diode detected the emission nearly perpendicular to the OLED device, while the emission has the angular distribution shown in *SI Appendix*, Fig. S1E. The light power density was determined by dividing the measured power by the emission area of the OLED cell (2 mm × 2 mm). The OLED was driven by DC voltages in the above measurements. The I-V characteristic for pulsed voltages was measured with amplitudes ranging from 5 to 20 V, a duration of 5 ms, and a frequency of 2 Hz (*SI Appendix*, Fig. S1D).

The characteristics of free-standing OLED attached to biological tissues were evaluated after delaminating the ultrathin OLED from the glass plate. The emitted-light intensity was monitored using a photodetector during a repetitive pulsed emission to evaluate the lifetime of the OLED (*SI Appendix*, Fig. S2 A and B). This was performed both with and without a 2-mm-thick extracted muscle tissue being placed on the OLED. The muscle tissue was thin enough to pass sufficient light from the OLED. The OLED was driven at an amplitude of 15 V, a pulse duration of 5 ms, and a frequency of 2 Hz.

Evaluation of Mechanical Damage to the Sciatic Nerve. Animal care and handling were conducted in accordance with the Guidelines of the Animal Experiment Committee at the University of Tokyo (approval numbers: KA12-1, KA12-4, KA13-3, and KA15-1) that follows the Notification on Animal Experimentation in Universities issued by the Ministry of Education, Culture, Sports, Science & Technology in Japan. Ten wild-type rats (Wistar, 220 to 260 g; 10 wk old) were used in the following experiments. C-shaped plastic cuffs representing existing rigid optical devices (54) with a length of 5 mm, an inner diameter of 1.5 mm, an outer diameter of 1.8 mm, and a gap of 1 mm were fabricated. The 2-μm-thick OLEDs were prepared with a width of 5 mm. These devices were sterilized by immersing the device in 70% ethanol solution for 15 min and cleaned using distilled water. When the sciatic nerve was exposed, the fascia and connective tissues around the nerve fiber were carefully removed. The rigid cuff was implanted into four rats by placing the cuff on the nerve. The OLED was implanted into four rats by wrapping the sciatic nerve with the OLED and fixed it using 6-0 polyester sutures at two places. The sham models of two rats were prepared by placing the rigid cuffs for 30 min under anesthesia and then removing them. After 10 d of implantation, the sciatic nerves were extracted after perfusion fixation using 4% paraformaldehyde phosphate buffer solution (Wako Pure Chemicals) and postfixed in the same fixative overnight. The extracted sciatic nerves were dehydrated and embedded in paraffin. The prepared samples were sliced transversely to a thickness of 3 μm at the proximal end of the implanted device and stained with Luxol fast blue (Muto Pure Chemicals). The longitudinal sections were prepared at the other end of the implanted device and applied for immunohistochemistry to stain macrophages. The primary antibody of mouse anti-rat CD68 monoclonal antibody (1/100; AbD Serotec) was used as a marker of macrophage. Primary antibodies were detected with Super Sensitive One-Step Polymer HRP (BioGenex). The background staining was performed with 0.05% toluidine blue (Muto Pure Chemicals). Macrophages, CD68-expressed cells, were counted in non-overlapped 10-section images for each sample. Damage to the nerve fibers in the three groups was assessed by statistical comparison of the numbers of CD68 positive cells. Using commercial software (JMP; SAS Institute Inc.), group–group differences were determined with a one-way ANOVA, followed by the Tukey–Kramer honestly significant difference (HSD) test at the 95% level of significance ($\alpha = 0.05$).

MRI Compatibility. The OLED was attached to the right hemisphere of the perfusion-fixed rat brain. An array of three GaN LEDs (KPHHS-1005QBC-D-V; Kingbright) was implemented on a flexible substrate of 1.4-μm-thick polyimide. The LEDs measured 1.2 mm × 0.8 mm, with a thickness of 0.5 mm. The devices were placed in the MRI system so that the normal of the substrate was perpendicular to the main static magnetic field (z direction). The RF

magnetic field was circularly polarized in the *xy* plane. The devices were not operated during MRI scan. T2-weighted images (Fig. 3*D*) were acquired using a rapid acquisition with a relaxation-enhancement sequence with the following parameters: repetition time (TR) = 2,500 ms; echo time (TE) = 33 ms; field of view (FOV) = 2 cm × 2 cm; 256 × 256 matrix; and 2-mm slice thickness. To investigate the signal attenuation on the OLED, a 1% agarose gel sample including the OLED was used. The images were acquired using fast low-angle shot sequences with TR = 350 ms, TE = 5.4 ms, flip angle = 40°, FOV = 1 cm × 3.2 cm, 256 × 256 matrix, and 4-mm slice thickness.

Animal Treatment during Surgery. We utilized a transgenic rat strain expressing ChR2-venus protein (W-TChR2V4 line; NBRP-Rat no. 0685) under the control of thy1.2 promoter (31). The animals were anesthetized with isoflurane for all of the surgeries reported in this paper (5% for induction and 2.0 to 2.5% for maintenance). The rectal temperature was monitored continuously using a digital thermometer, and a heating pad was used to maintain the body temperature at 37 °C.

Recording Electromyograms by Optical Stimulation of Nerve Terminal on the Gracilis Muscle. The rats (240 to 340 g; 10 to 13 wk old; *n* = 3) were anesthetized and the skin overlying the gracilis muscle on the medial side of the thigh was incised to expose the muscle. The nerve terminal on the muscle was identified using a laser (COME2-LB473/586/200S; LUCIR) administered through an optical fiber and scanned on the muscle belly, with a wavelength of 473 nm and light power density of ~2.5 mW/mm^2. The optical stimulations were delivered from the OLED at proximal positions on the muscle. The myoelectric potential was recorded using an amplifier (MEB-9104; Nihon Kohden Co.) through a pair of needle electrodes (NE-224S; Nihon Kohden Co.) inserted into the muscle. A ground electrode (25 mm × 45 mm; V-040M4; Nihon Kohden Co.) was attached on the contralateral skin. The OLED was driven in constant-voltage mode at 15 V with a pulse duration of 5 ms. The voltages were applied from a voltage-regulated power supply to the OLED. The voltages were switched using a transistor controlled by a pulse generator. Square-shaped pulses were applied with durations of 5 to 10 ms. To prevent drying of the muscle, the surface of the muscle was covered with an 11-µm-thick polymethylpentene sheet throughout the experiment.

Recording Electromyograms by Optical Stimulation of the Sciatic Nerve. The rats (220 to 340 g; 10 to 13 wk old; *n* = 2) were anesthetized, and the right sciatic nerve was exposed by dissecting the thigh and isolating the nerve from surrounding tissues for a length of 10 mm along the nerve. The OLED was inserted between the semimembranosus muscle and the vastus lateralis muscle and attached to the sciatic nerve. A pair of needle electrodes (NE-224S; Nihon Kohden Co.) was inserted into the gastrocnemius muscle, and the evoked electromyograms were measured using an amplifier (MEB-9104; Nihon Kohden Co.). The ground electrode was attached to the contralateral skin. The OLED was driven by 15 V with a 5-ms pulse duration and a repetition rate of two pulses per second.

Stimulation of Sensory Neurons. The rats (220 to 340 g; 10 to 13 wk old; *n* = 4) were anesthetized, and the heads were positioned on a stereotaxic frame. A craniotomy of 2.0 mm × 2.0 mm was performed, with the center 2.6 mm posterior and 2.2 mm right of the bregma, exposing the somatosensory cortex for the hindlimb (Fig. 2*F*). A needle electrode was inserted at the center of the craniotomy. We measured the potentials at needle-insertion depths of 0.6 mm. A hole of 2 mm in diameter was drilled in a symmetrical position on the contralateral hemisphere to insert a reference electrode. A silicone fixture for the reference electrode was bonded to the skull, and the tip of the reference electrode was located at a depth of 2 mm from the brain surface. To measure somatosensory-evoked potentials (SEPs), we placed the

animal, stimulator, and amplifier into an electromagnetically shielded box to reduce external noise. Both the OLED and amplifier (MED-A64HE1, MED-A64MD1; Alpha MED Scientific) were powered by batteries to eliminate power-line noise. Instead of using a digital thermometer and heating pad, the rats were placed on a warm-water circulator to minimize electrical noise. A bolus of α-chloralose (Sigma) was administered to the rats through the tail vein (60 mg/kg). After 10 min of bolus injection, isoflurane inhalation was stopped. After 30 min of bolus injection, anesthesia was maintained with continuous infusion of α-chloralose at 10 mg·kg^{-1}·h^{-1}. A pair of needle electrodes was inserted beneath the skin of the left hindlimb to provide reference electrical stimulations. We delivered a train of 300 pulsed stimulations with an intensity of 0.7 mA and a pulse duration of 300 µs. After removing the needle electrodes, the OLED device was attached to the skin and driven at 15 V with pulse durations of 5 and 10 ms. Every trial measurement was followed by a rest interval of 5 min. The SEP signals were amplified and band pass-filtered with cutoff frequencies ranging from 10 to 10,000 Hz. The SEP was processed using dedicated software (Mobius). The duration of each recording was 5 min.

fMRI Scans with Direct Brain Stimulation. fMRI scans were performed on two rats (220 to 260g; 10 wk old) using different optical-stimulation systems consisting of a fiber-coupled laser and an OLED. The rats were anesthetized with isoflurane and placed on a stereotaxic frame. A craniotomy of 4 mm × 4 mm was performed, with the center at 1.0 mm posterior and 3.0 mm lateral to the bregma on the left hemisphere, which exposed the cortex including the sensorimotor area. In the fMRI scan, the OLED fabricated on a 0.7-mm-thick glass plate was placed epidurally on the brain. For the fMRI scan using the fiber-coupled laser, the tip of the optical fiber (diameter, 250 µm) was placed on the cortical surface through a nonmagnetic cannula that was immobilized by a silicon rod and acrylic resin on the skull. The animal was catheterized through the tail vein and administrated an initial bolus of α-chloralose (60 mg/kg). Inhalation of isoflurane was reduced to 1% and stopped after 5 min. After placing the animal in the 7-T MRI system (BioSpec 70/20 USR; Bruker Co.), the anesthesia was maintained by continuously administering α-chloralose (10 mg·kg^{-1}·h^{-1}) during the MRI scan. A pilot image was obtained, and the slice positions for fMRI were determined to cover the directly stimulated area and the thalamus area (55). fMRI was performed with a block design, whereby one stimulation trial consisted of 60-s OFF, 30-s ON, and 60-s OFF. Optical stimulations of 3-Hz frequency and 5-ms pulse width were induced continuously for 30 s. The optical-power intensity was measured using an optical-power meter (Nova, P/N 7Z01500; OPHIR) in a steady-state illuminating condition. The optical-power intensity of OLED stimulation was ~2 mW (~0.5 mW/mm^2). In the fiber-coupled laser stimulation, the optical intensity at the tip was varied to be 2, 5, 12, and 20 mW. The echo planar imaging sequences were obtained with TR = 1,000 ms, TE = 13 ms, FOV = 3 cm × 3 cm, matrix = 64 × 64, and slice thickness = 2 mm. Data analysis was performed using statistical parametric mapping 8.0. The averaged rat brain template was used to map the evoked activities (56).

1. T. Someya, Z. Bao, G. G. Malliaras, The rise of plastic bioelectronics. *Nature* **540**, 379–385 (2016).
2. M. Kaltenbrunner *et al*., An ultra-lightweight design for imperceptible plastic electronics. *Nature* **499**, 458–463 (2013).
3. S. Wang *et al*., Skin electronics from scalable fabrication of an intrinsically stretchable transistor array. *Nature* **555**, 83–88 (2018).
4. D. Khodagholy *et al*., In vivo recordings of brain activity using organic transistors. *Nat. Commun.* **4**, 1575 (2013).
5. P. Leleux *et al*., Organic electrochemical transistors for clinical applications. *Adv. Healthc. Mater.* **4**, 142–147 (2015).
6. T. Yokota *et al*., Ultraflexible, large-area, physiological temperature sensors for multipoint measurements. *Proc. Natl. Acad. Sci. U.S.A.* **112**, 14533–14538 (2015).
7. M. Amjadi, A. Pichitpajongkit, S. Lee, S. Ryu, I. Park, Highly stretchable and sensitive strain sensor based on silver nanowire-elastomer nanocomposite. *ACS Nano* **8**, 5154–5163 (2014).
8. A. Pierre, A. Gaikwad, A. C. Arias, Charge-integrating organic heterojunction phototransistors for wide-dynamic-range image sensors. *Nat. Photonics* **11**, 193–199 (2017).
9. S. Takamatsu *et al*., Wearable keyboard using conducting polymer electrodes on textiles. *Adv. Mater.* **28**, 4485–4488 (2016).
10. D. Khodagholy *et al*., NeuroGrid: Recording action potentials from the surface of the brain. *Nat. Neurosci.* **18**, 310–315 (2015).
11. M. S. White *et al*., Ultrathin, highly flexible and stretchable PLEDs. *Nat. Photonics* **7**, 811–816 (2013).
12. T. Yokota *et al*., Ultraflexible organic photonic skin. *Sci. Adv.* **2**, e1501856 (2016).
13. M. Choi *et al*., Flexible active-matrix organic light-emitting diode display enabled by MoS2 thin-film transistor. *Sci. Adv.* **4**, eaas8721 (2018).
14. N. Obidin, F. Tasnim, C. Dagdeviren, The future of neuroimplantable devices: A materials science and regulatory perspective. *Adv. Mater.* **32**, e1901482 (2020).

15. C. M. Lochner, Y. Khan, A. Pierre, A. C. Arias, All-organic optoelectronic sensor for pulse oximetry. *Nat. Commun.* **5**, 5745 (2014).
16. J. T. Smith, B. O'Brien, Y. K. Lee, E. J. Bawolek, J. B. Christen, Application of flexible OLED display technology for electro-optical stimulation and/or silencing of neural activity. *IEEE/OSA J. Disp. Technol.* **10**, 514–520 (2014).
17. A. K. Bansal, S. Hou, O. Kulyk, E. M. Bowman, I. D. W. Samuel, Wearable organic optoelectronic sensors for medicine. *Adv. Mater.* **27**, 7638–7644 (2015).
18. A. Steude, E. C. Witts, G. B. Miles, M. C. Gather, Arrays of microscopic organic LEDs for high-resolution optogenetics. *Sci. Adv.* **2**, e1600061 (2016).
19. A. Morton, C. Murawski, S. R. Pulver, M. C. Gather, High-brightness organic light-emitting diodes for optogenetic control of Drosophila locomotor behaviour. *Sci. Rep.* **6**, 31117 (2016).
20. Y. Jeon et al., Sandwich-structure transferable free-form OLEDs for wearable and disposable skin wound photomedicine. *Light Sci. Appl.* **8**, 114 (2019).
21. E. S. Boyden, F. Zhang, E. Bamberg, G. Nagel, K. Deisseroth, Millisecond-timescale, genetically targeted optical control of neural activity. *Nat. Neurosci.* **8**, 1263–1268 (2005).
22. F. Zhang, A. M. Aravanis, A. Adamantidis, L. de Lecea, K. Deisseroth, Circuit-breakers: Optical technologies for probing neural signals and systems. *Nat. Rev. Neurosci.* **8**, 577–581 (2007).
23. X. Han et al., Millisecond-timescale optical control of neural dynamics in the non-human primate brain. *Neuron* **62**, 191–198 (2009).
24. L. Fenno, O. Yizhar, K. Deisseroth, The development and application of optogenetics. *Annu. Rev. Neurosci.* **34**, 389–412 (2011).
25. B. Y. Chow, E. S. Boyden, Optogenetics and translational medicine. *Sci. Transl. Med.* **5**, 177ps5 (2013).
26. S. I. Park et al., Soft, stretchable, fully implantable miniaturized optoelectronic systems for wireless optogenetics. *Nat. Biotechnol.* **33**, 1280–1286 (2015).
27. K. L. Montgomery et al., Wirelessly powered, fully internal optogenetics for brain, spinal and peripheral circuits in mice. *Nat. Methods* **12**, 969–974 (2015).
28. A. D. Mickle et al., A wireless closed-loop system for optogenetic peripheral neuromodulation. *Nature* **565**, 361–365 (2019).
29. J. H. Lee et al., Global and local fMRI signals driven by neurons defined optogenetically by type and wiring. *Nature* **465**, 788–792 (2010).
30. J. H. Lee, Informing brain connectivity with optogenetic functional magnetic resonance imaging. *Neuroimage* **62**, 2244–2249 (2012).
31. H. Wang et al., Molecular determinants differentiating photocurrent properties of two channelrhodopsins from chlamydomonas. *J. Biol. Chem.* **284**, 5685–5696 (2009).
32. H. Tomita et al., Visual properties of transgenic rats harboring the channelrhodopsin-2 gene regulated by the thy-1.2 promoter. *PLoS One* **4**, e7679 (2009).
33. T. Kuki et al., Frequency-dependent entrainment of neocortical slow oscillation to repeated optogenetic stimulation in the anesthetized rat. *Neurosci. Res.* **75**, 35–45 (2013).
34. D. Kim et al., "An MRI-compatible, ultra-thin, flexible stimulator array for functional neuroimaging by direct stimulation of the rat brain" in *36th Annual International Conference IEEE Engineering in Medicine Biology Society*, (IEEE, Chicago, IL, 2014), pp. 6702–6705.
35. Z. G. Ji et al., Light-evoked somatosensory perception of transgenic rats that express channelrhodopsin-2 in dorsal root ganglion cells. *PLoS One* **7**, e32699 (2012).
36. C. Towne, K. L. Montgomery, S. M. Iyer, K. Deisseroth, S. L. Delp, Optogenetic control of targeted peripheral axons in freely moving animals. *PLoS One* **8**, e72691 (2013).
37. V. C. Austin et al., Differences in the BOLD fMRI response to direct and indirect cortical stimulation in the rat. *Magn. Reson. Med.* **49**, 838–847 (2003).
38. A. P. Strafella, T. Paus, Cerebral blood-flow changes induced by paired-pulse transcranial magnetic stimulation of the primary motor cortex. *J. Neurophysiol.* **85**, 2624–2629 (2001).
39. O. Yizhar, L. E. Fenno, T. J. Davidson, M. Mogri, K. Deisseroth, Optogenetics in neural systems. *Neuron* **71**, 9–34 (2011).
40. J. M. Stujenske, T. Spellman, J. A. Gordon, Modeling the spatiotemporal dynamics of light and heat propagation for in vivo optogenetics. *Cell Rep.* **12**, 525–534 (2015).
41. A. N. Yaroslavsky et al., Optical properties of selected native and coagulated human brain tissues in vitro in the visible and near infrared spectral range. *Phys. Med. Biol.* **47**, 2059–2073 (2002).
42. R. H. Kim et al., Waterproof AlInGaP optoelectronics on stretchable substrates with applications in biomedicine and robotics. *Nat. Mater.* **9**, 929–937 (2010).
43. T. I. Kim et al., Injectable, cellular-scale optoelectronics with applications for wireless optogenetics. *Science* **340**, 211–216 (2013).
44. K. Y. Kwon, B. Sirowatka, A. Weber, W. Li, Opto-μECoG array: A hybrid neural interface with transparent μECoG electrode array and integrated LEDs for optogenetics. *IEEE Trans. Biomed. Circuits Syst.* **7**, 593–600 (2013).
45. J. G. McCall et al., Fabrication and application of flexible, multimodal light-emitting devices for wireless optogenetics. *Nat. Protoc.* **8**, 2413–2428 (2013).
46. I. Diester et al., An optogenetic toolbox designed for primates. *Nat. Neurosci.* **14**, 387–397 (2011).
47. X. Han, Optogenetics in the nonhuman primate. *Prog. Brain Res.* **196**, 215–233 (2012).
48. A. Gerits et al., Optogenetically induced behavioral and functional network changes in primates. *Curr. Biol.* **22**, 1722–1726 (2012).
49. A. Gerits, W. Vanduffel, Optogenetics in primates: A shining future? *Trends Genet.* **29**, 403–411 (2013).
50. X. Dai, Y. Deng, X. Peng, Y. Jin, Quantum-dot light-emitting diodes for large-area displays: Towards the dawn of commercialization. *Adv. Mater.* **29**, 1607022 (2017).
51. M. K. Choi et al., Extremely vivid, highly transparent, and ultrathin quantum dot light-emitting diodes. *Adv. Mater.* **30**, 1703279 (2018).
52. A. Stroh et al., Tracking stem cell differentiation in the setting of automated optogenetic stimulation. *Stem Cells* **29**, 78–88 (2011).
53. T. Asano, T. Ishizuka, K. Morishima, H. Yawo, Optogenetic induction of contractile ability in immature C2C12 myotubes. *Sci. Rep.* **5**, 8317 (2015).
54. M. E. Llewellyn, K. R. Thompson, K. Deisseroth, S. L. Delp, Orderly recruitment of motor units under optical control in vivo. *Nat. Med.* **16**, 1161–1165 (2010).
55. G. Paxinos, C. Watson, *The Rat Brain in Stereotaxic Coordinates*, (Academic Press, ed. 7, 2013).
56. P. A. Valdés-Hernández et al., An in vivo MRI template set for morphometry, tissue segmentation, and fMRI localization in rats. *Front. Neuroinform.* **5**, 26 (2011).